ELSEVIER

Contents lists available at ScienceDirect

Chemical Engineering Journal

journal homepage: www.elsevier.com/locate/cej





Efficient electrochemical CO₂ reduction to CO by metal and nitrogen co-doped carbon catalysts derived from pharmaceutical wastes adsorbed on commercial carbon nanotubes

Yang Gang ^a, Boyang Li ^b, Siyuan Fang ^c, John Pellessier ^a, Lingzhe Fang ^d, Fuping Pan ^a, Zichen Du ^a, Yun Hang Hu ^c, Tao Li ^{d,e}, Guofeng Wang ^b, Ying Li ^{a,*}

- ^a J. Mike Walker '66 Department of Mechanical Engineering, Texas A&M University, College Station, Texas 77843, United States
- b Department of Mechanical Engineering and Materials Science, University of Pittsburgh, Pittsburgh, PA 15261, United States
- ^c Department of Materials Science and Engineering, Michigan Technological University, Houghton, MI 49931, United States
- ^d Department of Chemistry and Biochemistry, Northern Illinois University, DeKalb, IL 60115, United States
- ^e Chemistry and Material Science Group, X-ray Science Division, Argonne National Laboratory, Lemont, IL 60439, United States

ABSTRACT

Transition metal and nitrogen doped carbon catalysts (M—N—C) are effective in electrochemical reduction of CO_2 to CO with a high selectivity. However, scalable and cost-effective synthesis of active metal-nitrogen catalysts is yet to be developed. Herein, we report a simple and sustainable method that utilizes commercial carbon nanotubes (CNTs) to adsorb a pharmaceutical waste, sulfamethoxazole (SMX), followed by moderate pyrolysis to prepare an efficient M—N—C catalyst. The intrinsic metal impurities from CNTs are essential to form active metal sites, and it requires significantly less nitrogen precursor than methods using most widely nitrogen precursors such as melamine and urea. The CNT-SMX catalyst delivers high CO_2RR performance with 91.5 % CO Faradaic efficiency and 14 mA/cm² CO partial current density at -0.76 V vs RHE in a traditional H-Cell. The catalyst is also efficient in a scalable flow cell, exhibiting 97.5 % CO selectivity at 300 mA/cm², plus stable CO_2RR performance for more than 24 h at 100 mA/cm². The scanning transmission electron microscopy (STEM) and X-ray absorption spectroscopy (XAS) analyses confirm the existence of single atomic sites primarily in the form of Fe-N bonds that are active sites for CO_2RR . Density functional theory (DFT) calculations suggest a synergy between the single atomic Fe—N—C sites and Ni nanoparticles embedded in the CNTs, which enhances CO production rate and selectivity by lowering the desorption energy of *CO intermediate. To the best of our knowledge, the results in this work are among the top performing carbon-based catalysts. Furthermore, catalysts developed in this work are synthesized at a moderate temperature without pre-oxidation or post-acid-washing and utilize cheap or waste materials, presenting a simple, sustainable, and cost-effective way to synthesize highly active catalysts.

1. Introduction

The electrochemical CO_2 reduction reaction (CO_2RR) is a promising solution to mitigate excess CO_2 concentration in the atmosphere that results in global warming [1,2]. Utilizing renewable energy such as solar and wind as the electricity source, CO_2RR can produce value-added chemicals at mild reaction conditions with significant scale-up potentials of the entire process. However, CO_2RR normally suffers from sluggish reaction rates due to the stable nature of CO_2 molecules. Thus, the reaction requires highly efficient catalysts to reduce the reaction barrier and boost the activity to a practical level.

Among the many catalysts researched, metal and nitrogen co-doped carbon (M—N—C) has attracted increasing attention because of its advantageous properties including cost-effectiveness, abundance of precursor materials, and potential for large-scale application [3,4]. Two

types of carbon precursors are typically used to synthesize M—N—C catalysts. One starts from functionalized pristine carbon such as graphene oxide, carbon nanotubes (CNT), or carbon black, followed by doping nitrogen and metal sources at high temperature [5–7]. The other route begins with carbon/nitrogen/metal-containing organic-based precursors, which are subjected to the high-temperature pyrolysis [8–10]. Typically, multiple pre-treatments, namely strong acid/oxidant activations, are used in order to provide high carbon surface area and achieve effective nitrogen/metal doping [6,11,12]. In terms of the metal precursor, metal salts (e.g., metal nitrates) are normally used for metal doping. Since the aggregation of metal sites, which forms metal nanoparticle on the carbon matrix during pyrolysis, decreases CO₂RR performance because of favoring competing hydrogen evolution reaction (HER) [13], post-pyrolysis acid washing is typically applied to achieve a uniform distribution of M—N sites [8,14,15]. These treatments not only

E-mail address: yingli@tamu.edu (Y. Li).

 $^{^{\}ast}$ Corresponding author.

hinder the scale-up potential of the synthesis, but also produce pollutants, further adding the burden of downstream waste treatment to the CO₂RR life cycle.

Furthermore, in order to anchor nitrogen onto the carbon matrix, extensive amounts of nitrogen sources (such as urea, melamine, etc.) are typically used at quantities more than ten times the weight of the carbon source. However, the poor interaction between these precursors and carbon precursors results in a majority of the nitrogen elements escaping as gasses instead of being doped onto the carbon [5–7,16]. This leads to a low product yield considering the carbon/nitrogen quantity ratio, thus significantly reducing the scale-up potential and cost-effectiveness of the M—N—C catalyst synthesis. As a result, low-cost carbon, metal, and nitrogen sources requiring fewer treatment steps while still being effective for constructing M—N active sites are needed for future large-scale applications of $\mathrm{CO}_2\mathrm{RR}$ catalyst synthesis.

Multi-walled carbon nanotubes (CNTs) are one of the most popular carbon precursors researched [11,17-19]. It has been synthesized in an industrial scale and is more cost-effective than the other synthesized carbon precursors, such as graphene or metal-organic-frameworks (MOFs). CNTs also have a larger surface area, better conductivity, and greater strength than the natural carbon sources, such as graphite [20–22]. However, the majority of the literature reports using CNTs solely as the carbon precursor suffer from multiple aforementioned disadvantages due to pre-/post-pyrolysis treatments [19,23,24]. As demonstrated in our previous work, the metal impurities often found in CNTs from the industrial synthesis can be utilized as the metal precursors for the M-N-C catalyst, eliminating the additional metal requirement and post-pyrolysis acid-washing [7]. This makes the commercial CNTs a potential candidate to be directly applied in a 'greener' synthesis with fewer pollutant treating steps when given the suitable nitrogen precursors.

Regarding nitrogen precursor selection, the use of traditional nitrogen sources such as urea and melamine requires an excessive amount to guarantee sufficient doping, making it a less sustainable synthesis. In contrast, common pharmaceutical products (e.g., sulfamethoxazole (SMX)), which also contain nitrogen elements, have been demonstrated to have a strong interaction with carbon materials in water due to π - π bonding [25–28]. This would make these materials a better candidate as M-N-C nitrogen precursors than traditional smaller nitrogencontaining molecule (e.g., urea, melamine, etc.) because they uniformly bond throughout the carbon surface, thus having a larger chance during pyrolysis to react with the metal impurities found in CNT and form M-N active sites. In addition, the over treatment of live-stock with these antibiotics has led to an increase of pharmaceutical wastes in water sources as well as existing as solid wastes [29]. Notably, these organics also contain elements such as S, Cl, or F, which were demonstrated to boost the activity of M—N—C catalysts further [8,30,31]. The

utilization of these organics as heteroatom dopants could not only enhance the cost-effectiveness of M—N—C synthesis, but also potentially contributes to the waste treatment of water or landfills.

In this work, a simple and sustainable method of M—N—C catalyst synthesis was developed as illustrated in Fig. 1. First, commercial CNTs were used to adsorb SMX from a solution. Then, the organics adsorbed CNTs were collected and underwent a moderate temperature pyrolysis to prepare atom-level dispersed M—N—C catalysts. The $\rm CO_2RR$ performance of the prepared catalysts was comprehensively characterized and evaluated in both an H-Cell and a flow cell. The results show a top-level catalytic performance while the amount of nitrogen precursors for the catalyst preparation is significantly reduced, and the procedures are simplified compared to other methods reported in the literature.

2. Experiment section

2.1. Materials

SMX (Tokyo Chemical Industry, > 98 %) and melamine (Acros Organics, > 99 %) were purchased from VWR. All chemicals were used directly without any treatment.

2.2. SMX adsorption

In this work, we dissolved SMX in water to simulate an SMX wastewater in the concentration range of 20–250 ppm (or mg/L). Typically, 50 mg of commercial CNT were dispersed into 50 mL of a SMX solution (20–250 ppm) under stirring at 300 rpm and room temperature. At certain time intervals, 1 mL of solution was taken out for analysis. CNT powders with adsorbed SMX were filtered out by a 45 nm PTFE filter. The liquid samples were diluted by 100 times for HPLC detection of SMX. The adsorption capacity was calculated based on the following equation:

$$Q_e = V_O * \frac{C_O - C_C}{m_{CNT}} \tag{1}$$

In this equation, V_O represents the volume of the organic solution, C_O is the original organic concentration, C_C is the current SMX concentration at the time the 1 mL sample was removed, and m_{CNT} is the mass of CNT.

The organic adsorption isotherm was plotted using the equilibrium organic concentration (C_e) as the x-axis and the adsorbed quantity (Q_e) as the y-axis.

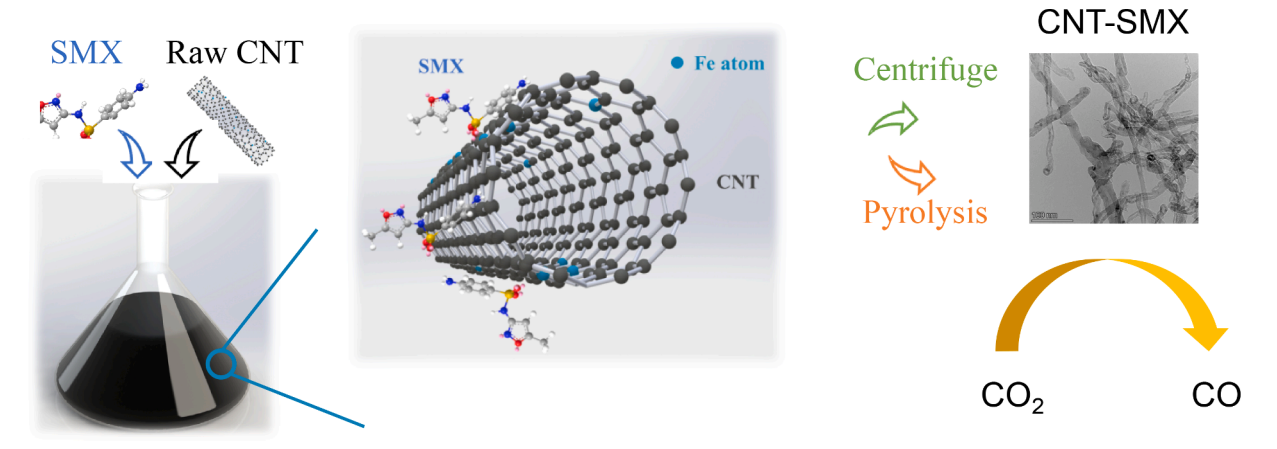


Fig. 1. The process of fabricating M—N—C catalysts using commercial CNTs and organic wastes for the application of CO₂RR.

2.3. Synthesis of catalysts

2.3.1. CNT-SMX-x

To begin 50 mg of commercial CNTs without treatment (denoted as CNT) was added to 50 mL of an X ppm SMX solution (X=20-250) and stirred at 300 rpm for 24 h. The CNT adsorbed with SMX was collected by centrifuging, pouring off the supernatant, and then dry at the 60 °C oven overnight. The dried powders were then pyrolyzed at 650 °C for 3 h under an Ar environment. The as-prepared powder was denoted as CNT-SMX-X.

2.3.2. CNT-HT

The control sample CNT-HT was synthesized by pyrolyzing 50 mg of CNT at 650 °C for 3 h under an Ar environment.

2.3.3. CNT-Mel-250

To compare the nitrogen doping level on CNT between SMX and the traditional precursor (melamine is selected in this work), CNT-Mel-250 was prepared using the same method except replacing 250 ppm of SMX solution by 250 ppm of melamine.

2.3.4. CNT-Mel-excessive

In order to achieve a similar nitrogen doping level and CO_2RR performance using melamine as the nitrogen precursor to that from SMX, excessive amount of melamine was used with similar carbon/nitrogen precursor weight ratio to the literature (at least 1:10) [7,32]. Typically, 50 mg of CNT and 500 mg of melamine were dispersed in 20 mL DI water. The water was then fully evaporated on a hotplate at 60 °C. The as-mixed power was then transferred to a tube furnace and pyrolyzed at 650 °C for 3 h under an Ar environment. The as-synthesized sample is denoted as CNT-Mel-excessive.

2.4. Characterizations

2.4.1. Morphology, structure, and composition of the catalysts

Morphology, structure, and composition of the catalysts were characterized by scanning electron microscopy (SEM, JEOL JSM7500F), transmission electron microscopy (TEM, FEI Tecnai G2 F20 ST), Brunauer-Emmett-Teller (Micromeritics ASAP 2420 physisorption analyzer), high-angle angular dark-field scanning transmission electron microscopy (FEI 200 kV Titan Themis), X-ray diffraction (XRD, BURKER D8), and X-ray photoelectron spectroscopy (XPS, Omicron). The X-ray absorption spectroscopy (XAS) measurements were performed at the 12-BM beamline of the Advanced Photon Source (APS) at the Argonne National Laboratory (ANL).

2.4.2. Measurement of the SMX concentration

The concentration of SMX was measured by high-performance liquid chromatography (HPLC-2030C, Shimadzu) equipped with a reversed-phase C18 column in the low-pressure gradient mode. A mixture of deionized water, acetonitrile, and 25 mM of formic acid was used as the mobile phase at a flow rate of 1 mL/min.

2.5. Electrochemical CO₂RR activity measurements

Two types of cells were used in this work to evaluate the CO_2RR performance. A traditional H-Cell was used to conduct electrochemical characterizations and study fundamental catalytic performance-structure correlations. A flow cell setup was used to analyze the scale-up potentials of the catalyst while operating at higher current densities.

2.5.1. H-Cell

The traditional H-Cell contains two compartments, separated by a proton exchange membrane (Nafion 115 membrane, Beantown Chemical, 0.125 mm thick). It is a three-electrode system, consisting of a working electrode and a reference electrode (Ag/AgCl, 3 M KCl) in the

cathode chamber, and a counter electrode (1 cm \times 1 cm Pt foil) in the anode chamber. The electrolyte is the CO_2 -saturated 0.5 M KHCO $_3$ solution. The measured potentials after iR compensation are rescaled to the reversible hydrogen electrode by E (RHE) = E (Ag/AgCl) + 0.210 V + 0.0591 V \times pH. The working electrode is prepared by drop-casting the catalyst onto a Toray carbon paper with an active catalytic geometric area of 1 cm 2 . The catalyst ink is prepared by dispersing 3 mg of catalysts in a mixture of 370 μL of ethanol, 200 μL of water, and 30 μL of 5 % Nafion solution under sonication for 3 h. High-purity CO $_2$ (99.999 %, Airgas) at a flow rate of 30 standard cubic centimeters per minute (sccm) is introduced in the cathode chamber for 30 min to fully saturate the catholyte and the flow rate is maintained throughout the test. The products are analyzed via an online gas chromatograph (GC, Fuel Cell GC-2014ATF, Shimadzu) equipped with a thermal conductivity detector (TCD) and a methanizer-assisted flame ionization detector (FID).

2.5.2. Flow Cell

Similar to our previous work, a customized flow cell electrolyzer is used to evaluate the feasibility of applying the catalyst at commercially viable current densities [33]. The flow cell has two compartments separated by an anion exchange membrane (Fumasep PK 130, Fuel Cell Stores). Nickel foam is used as the anode for oxygen evolution reaction (OER) with an active geometric area of 1 cm², and the analyte (1 M KOH) is circulated in the anode chamber (flow rate 10 mL/min) and remove the oxygen generated at the anode. The catholyte (1 M KOH) is circulated in the cathode chamber between the membrane and cathode at a flow rate of 1.5 mL/min. The cathode is prepared by airbrushing the catalyst ink (10 mg catalyst, 3 mL ethanol, 300 µL of 5 % Nafion solution) onto the gas diffusion layer (GDL) (Sigracet 39 BC, Fuel Cell Store) with an active geometric area of 1 cm². The catalyst loading is about 1 mg/cm² based on the electrode weight gain after airbrushing. The CO₂ gas, circulated at the backside of the GDL, diffuses into the GDL, and reacts at the catalyst-electrolyte interface. A Hg/HgO electrode (1 M KOH) is used as the reference. The flow cell tests were powered by a DC power supply (Agilent E3633A) and the potential between the reference and cathode is measured by a multimeter (AidoTek VC97 +). All the measured potentials were reported without iR compensation. The products in the flow cell systems are analyzed via an online gas chromatograph (GC, GC-2010, Shimadzu) equipped with a thermal conductivity detector (TCD) and flame ionization detector (FID). Both CO and H2 are detected by the TCD, and methane and hydrocarbons are measured by the FID detector.

3. Results and discussions

3.1. Adsorption kinetics and isotherm

Detailed analysis of different organic adsorption characteristics by CNT was investigated. The adsorption kinetics were determined by the adsorption capacity of organics onto CNT via time. The adsorption capacity of CNT rapidly reached its maximum within 10 min as shown in Figure S1 indicating the efficient and fast adsorption capability on commercial raw CNT [34].

To further understand the interactions between organics and CNT, adsorption isotherms were carried out and fitted with multiple isotherm models. As revealed in Fig. 2 and Table S1, different models are fitted well to the experimental data. In particular, the Freundlich model was better fitted to the experimental results than Langmuir model, indicating a multilayer adsorption of SMX molecules onto the heterogeneous CNT surface [35,36]. The efficient adsorption of SMX by CNT provides a good interaction between CNT and SMX, benefiting the following nitrogen doping step during pyrolysis.

3.2. Material characterization

Inductively coupled plasma mass spectrometry (ICP-MS) was first

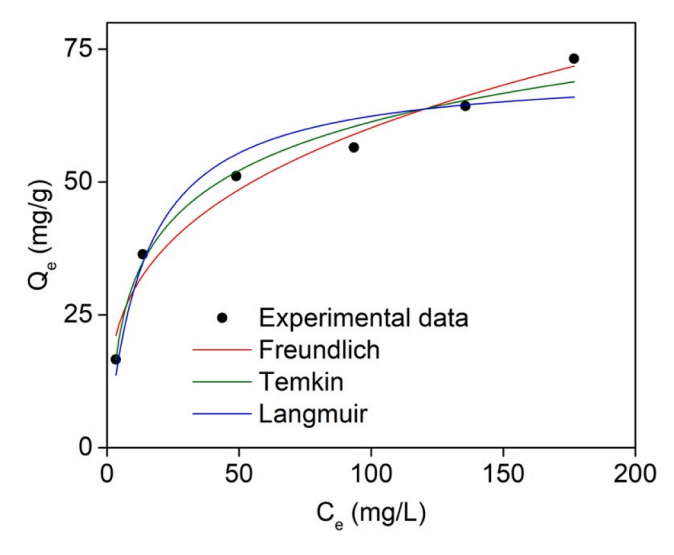


Fig. 2. SMX adsorption isotherm with different fitting models (Q_e : adsorption capacity; C_e : solution concentration at equilibrium).

conducted to understand the concentrations of residual Fe and Ni remained from the industrial synthesis process in CNT, CNT-HT, and CNT-SMX-250. As revealed in Table S2, the precursor CNT has 0.4 wt% and 1.0 wt% of Fe and Ni, respectively. After adsorption and pyrolysis, the catalyst CNT-SMX-250 has 0.4 wt% of Fe and 1.5 wt% of Ni. The control CNT-HT has 0.3 wt% of Fe and 1.7 wt% of Ni, respectively. These

results indicate that metals are preserved after the adsorption/pyrolysis processes.

Multiple characterization techniques are used to further understand the material structure, morphology, and element composition. Firstly, scanning electron microscope (SEM) was carried out to determine the structure differences between CNT and CNT-SMX-250. From Figure S2, all samples depict tube structures with similar diameters and lengths, indicating the structure of CNT well preserved after the pyrolysis. Transmission electron microscope (TEM) of CNT-SMX-250 (Fig. 3a) and CNT (Figure S3) reveal a similar tube structure with nanoparticles being encapsulated at the joint of tubes. In Figure S4, the encapsulation of a Ni nanoparticle by carbon layers is revealed by high-resolution TEM in CNT-SMX-250. As shown in Fig. 3b, high angle annular dark-field aberration-corrected scanning transmission electron microscopy (HAADF-STEM) reveals scattered bright spots, indicating the single atomic metal sites. Further energy dispersive spectroscopy (EDS) mapping (Fig. 3c-g) reveals uniform distribution of Fe elements, while Ni elements concentrated inside the tubes, forming nanoparticles. This indicates that the Fe sites more likely form smaller atomic sites while Ni elements exist in the system as nanoparticles. In particular, small nanoparticles could also be observed in the high-resolution STEM image (Fig. 3b). From the EDS spectrum to the red-square area of Fig. 3b, it is revealed that the nanoparticles consist of Ni elements primarily (Figure S5). The STEM and EDS images of commercial CNTs are revealed in Figure S6. Bright dots are also observed from the precursor CNT indicating the existence of single atomic sites in the raw CNTs without treatment. As demonstrated by the literature, Fe elements could form stable sites as isolated atoms on the defects of CNT surface while Ni elements are more likely to diffuse instantaneously and form aggregates [37]. This is consistent to

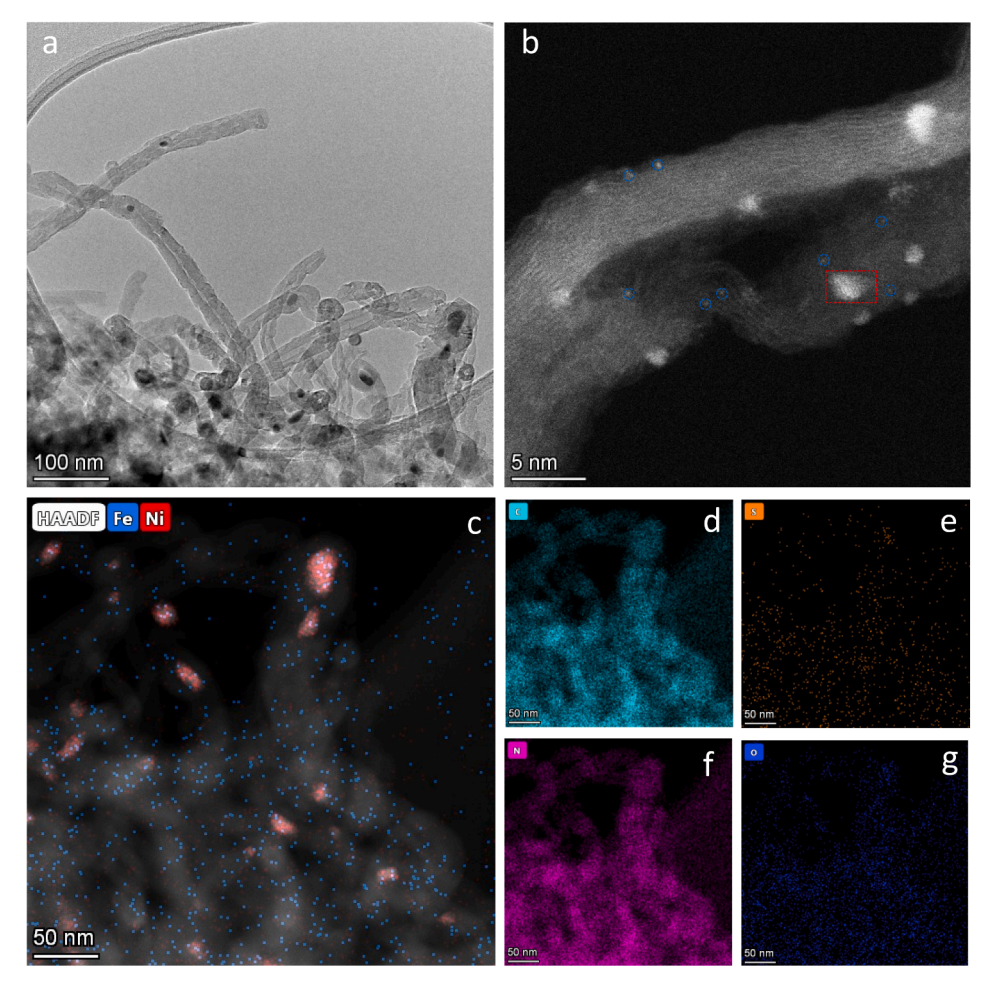


Fig. 3. (a) TEM and (b-g) HAADF-STEM/EDS images of CNT-SMX-250.

the EDS observation (Fig. 3c) where majority of Ni exist as nanoparticles in the system.

Brunauer-Emmett-Teller (BET) was conducted to determine the porosity and pore size distribution of CNT and CNT-SMX-250. As shown in **Figure S7**, both CNT and CNT-SMX-250 reveal a distinct hysteresis loop in the larger pressure range (P/P0 greater than 0.5), corresponding to mesopores [38]. CNT-SMX-250 also has a stronger absorption in the low relative pressure range (P/P0 = 0–0.1), indicating the existence of micropores [38]. The BET specific surface area of CNT-SMX-250 is $170.6~\text{m}^2/\text{g}$, larger than that of CNT, $81.1~\text{m}^2/\text{g}$. It is likely due to the formation of metal and nitrogen doped sites on the CNT surface provided by the introduction of SMX, creating rough defects and more porous surfaces than the pristine CNTs, agreeing with the literature finding [39]. The pore size distributions of the two samples are similar with a major pore size in the mesopore range at around 3 nm.

To better understand the surface metal composition and distribution, X-ray photoelectron spectroscopy (XPS) was further conducted. Differing from the results of ICP, the surface concentrations of Ni and Fe do not show a similar trend. As depicted in Table S3, the Ni contents in all samples are extremely low, less than 0.05 at.%, indicating the Ni contents exist mostly as nanoparticles that are encapsulated by the carbon layers other than exposed on the surface, consistent with the STEM/EDS observation. The surface Fe content in the CNT is much larger than that of Ni, around 0.5 at.% vs 0.05 at.%. This indicates that after the industrial process, larger quantities of Fe elements distribute on the surface, while Ni elements exist as nanoparticles encapsulated by graphitic carbon layers. This observation is consistent to the literatures, where Fe elements could form isolated atoms on the CNT surface while Ni elements tend to instantaneously form aggregates [7,37,40]. This leads to a higher Fe concentration than that of Ni on the surfaces of CNT and CNT-SMX-250 even if Ni has higher bulk concentrations as detected by ICP-MS (Table S2). The surface Ni contents in both CNT and CNT-SMX-250 are less than 0.05 at.%, indicating Ni nanoparticles are encapsulated after pyrolysis, agreeing with the STEM/EDS observations. Combining TEM/ICP/XPS observations, the surface metal elements that exist in the system are primarily single atomic Fe while Ni elements mostly exist as nanoparticles encapsulated by the graphitic carbon layers.

Furthermore, surface element concentrations of heteroatoms are revealed in Table S3. CNT has a larger surface O concentration, 9.4 at. %, as compared to CNT-SMX-250, 3.7 at.%. This is possibly due to the adsorption of O-containing species or the oxidation of surface iron species in CNT during storage. No obvious N or S could be detected from CNT, while 0.8 and 0.2 at.% of N and S are detected in CNT-SMX-250, respectively, indicating the successful heteroatom doping by introducing SMX.

High-resolution N 1 s spectra of CNT-SMX-250 (Figure S8) reveals the presence of five different N species, including pyridinic N (398.2 eV), metal-N (M-N) (399.5 eV), pyrrolic N (400.3 eV), graphitic N (401.2 eV), and N-oxides (403.7 eV) [6]. The presence of the M-N content reveals the formation of metal-nitrogen bond. Particularly, the M-N species dominate the N contents, indicating the effectiveness of forming M-N bonds using SMX as the N precursor. The formation of a large amount of M-N bonds is possibly because the surface Fe atoms have already been stabilized as isolated sites by the industrial fabrication process, while the uniform distribution of SMX molecules on the CNT surfaces provides effective formation of Fe-N bonds. As revealed in Figure S9, the S 2p spectra of CNT-SMX-250 at lower binding energy can be assigned to C—S—C ($2p_{3/2}$ at 164.1 and $2p_{1/2}$ at 165.3 eV), and the peaks centered at 167.6 and 168.8 eV correspond to oxidized species (C-SOx-C) [41-43]. Our previous work has demonstrated that the incorporation of S atoms could boost the CO2RR activity in the nitrogen doped carbon catalyst system by decreasing the reaction barrier of intermediate formation and promoting the active nitrogen species [41]. This further demonstrates the advantages of using SMX and CNT as raw precursors for M-N-C synthesis. In contrast, the commercial CNTs reveals no N peak (Figure S10), indicating no N exists in the raw materials.

In addition, high-resolution XPS analysis of metal species in CNT and CNT-SMX-250 are shown in Figure S11. Both samples reveal similar Fe spectra, indicating no significant changes of Fe after pyrolysis. As shown in Figure S11, both Fe peaks show a shift towards higher binding energy compared to the standard Fe⁰ value, suggesting a positive oxidation state [44–46]. In contrast, the XPS of Ni spectrum of raw CNTs does not show any obvious peak due to the extremely low concentration (less than 0.05 at.%, Table S3) on the surface, because Ni NPs are wrapped by carbon layers. After pyrolysis with SMX, a small Ni peak occurs at around 855 eV, likely due to the formation of Ni-N sites, with an oxidation state larger than 0 [47].

To further understand the local arrangement of metal atoms, X-ray absorption spectroscopy (XAS) was conducted on CNT-SMX-250. Fe foil, Fe₂O₃, Ni foil, iron phthalocyanine (FePc), and nickel phthalocyanine (NiPc) were used as the standards. The X-ray absorption near edge structure (XANES) spectra of Ni (Fig. 4a) in CNT-SMX-250 are all close to Ni foil, indicating a dominating Ni⁰ state. Notably, the edge of Ni in CNT-SMX-250 is slightly larger than 0, indicating some Ni elements possibly form Ni-N or Ni-O bonds. As shown in Fig. 4b, extended X-ray absorption fine structure (EXAFS) spectra of Ni atoms reveal a single peak at around 2 Å, close to Ni-Ni peak in Ni foil. No other Ni peaks are found, indicating the dominating Ni structure in CNT-SMX-250 being Ni nanoparticles, consistent with the STEM results (Fig. 3c). This is consistent with the XRD observation (Figure S12) where a metal nanoparticle peak appears at around 45°.

In contrast, the XANES spectra of Fe (Fig. 4c) shows different Fe oxidation state in CNT-SMX-250. CNT-SMX-250 reveals an adsorption edge profile between Fe foil and Fe₂O₃, indicating a Fe oxidation state in CNT-SMX-250 between 0 and 3+, in consistent to the XPS results (Figure S11) [48,49]. This is possibly due to the formation of Fe-N bonds as revealed by literature, where the Fe oxidation state is found to be close to 2+ in the Fe—N—C materials [7,50,51].

Moreover, as shown in Fig. 4d, CNT-SMX-250 exhibits a peak at around 1.5 Å, corresponding to either Fe-N in FePc or Fe-O in Fe $_2$ O $_3$. Notably, CNT-SMX-250 also shows a peak at around 2.2 Å, possibly corresponding to Fe-Fe peak in Fe foil or bimetallic Ni-Fe peak [52]. This is consistent to the observation of STEM/EDS (Figure S5) where Fe peak intensity can be observed, indicating a small quantity of Fe element in the Ni nanoparticles.

Since Ni and Fe elements exist in the system based on the ICP/EDS/XPS results, it is impossible to exclusively exclude Ni atomic site formation. As a result, it is hypothesized that the nanoparticle structure primarily consists of Ni elements with small quantities of Fe while the atomic sites primarily consist of Fe-N sites with small quantities of Ni [3,8,53]. These nanoparticles are encapsulated in the CNT branch/tip and are preserved even after an industrial acid purification process that removes the exposed metal nanoparticles.

3.3. CO₂RR performance evaluation

3.3.1. Traditional H-Cell

The CO₂RR performance of the as-prepared catalysts was firstly evaluated in a traditional H-Cell. The Faradaic efficiency of CO (FE(CO)) of CNT-SMX-*X* and CNT-HT at different applied potentials are depicted in Fig. 5a. The highest FE(CO) of CNT-SMX-*X* is achieved at -0.76 V vs RHE of 91.5 % with a partial CO current density of 14 mA/cm² (Fig. 5b-c) by CNT-SMX-250. As concentration of precursor SMX solution increases, FE(CO) and current density of CNT-SMX-*X* increase. FE(CO) and current density in all CNT-SMX-X are significantly larger than that of CNT-HT, 1.6 % of FE(CO) with a CO current density of 0.02 mA/cm². This demonstrates the significance of Fe-N active sites formed by SMX adsorption/pyrolysis process. Since the physical properties of CNT-SMX-*X* samples and pristine CNTs (e.g., BET surface area, structure, etc.) are similar, the differences are more likely due to the nitrogen doping level

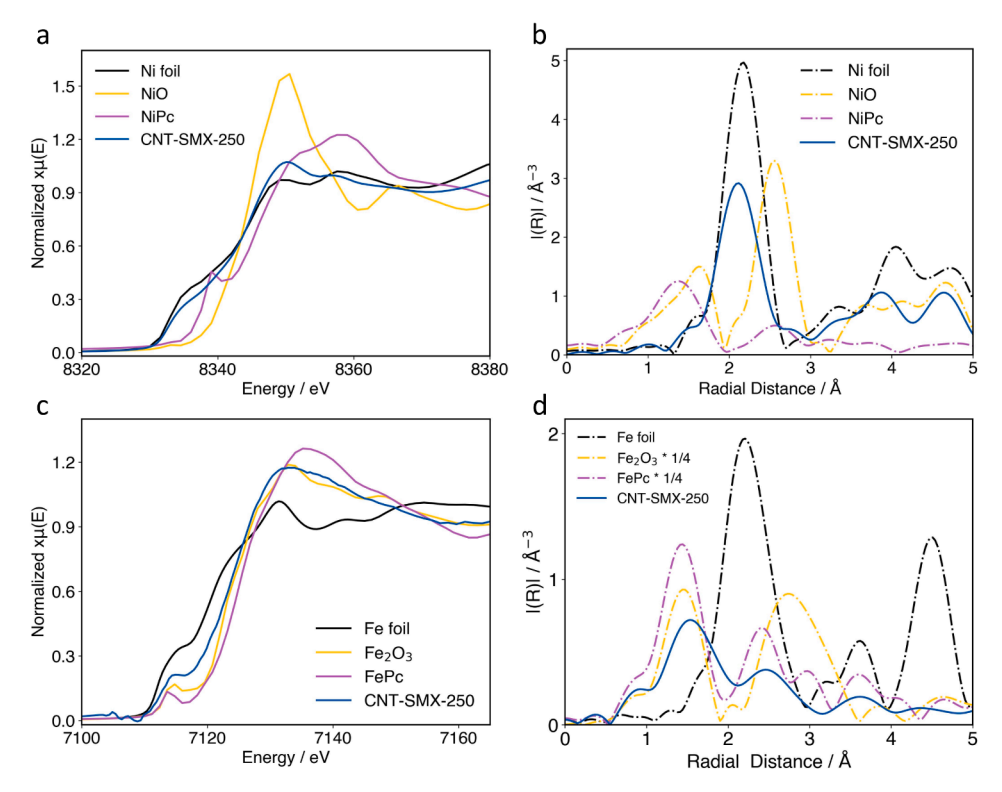


Fig. 4. (a) Ni XANES, (b) Fourier transform of the Ni EXAFS spectra, (c) Fe XANES, and (d) Fourier transform of the Fe EXAFS spectra of CNT-SMX-250 and standard references.

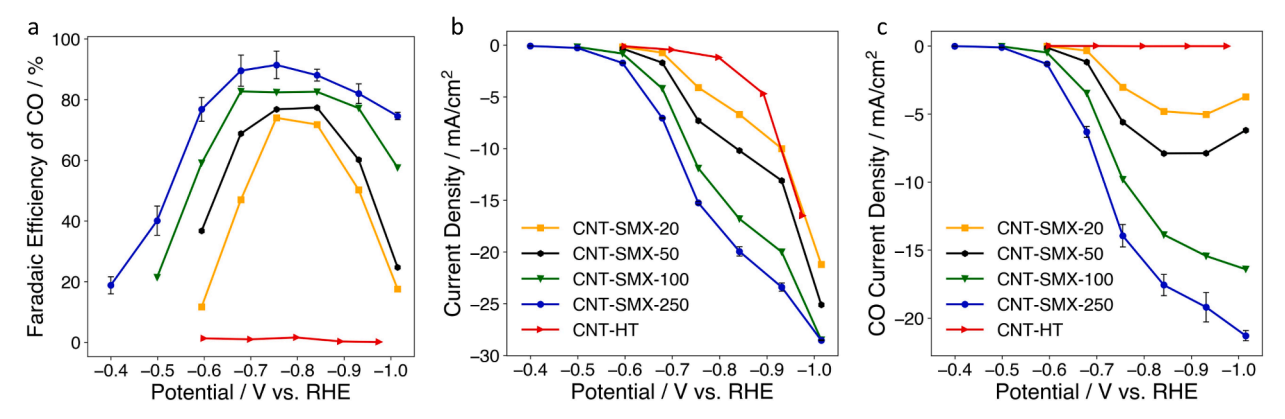


Fig. 5. (a) CO Faradaic efficiency, (b) total current density, and (c) CO partial current density on CNT-SMX-X and CNT-HT in 0.5 M KHCO₃

resulted from different SMX adsorption quantities. As shown in Fig. 2, the SMX equilibrium adsorption capacity (Qe) by CNTs in the 250-ppm SMX solution (corresponds to CNT-SMX-250 in Fig. 5) is about 1.5 times of that in the 100-ppm solution (CNT-SMX-100), and 5 times of that in the 20-ppm solution (CNT-SMX-20). In comparison, CNT-HT (i.e., CNT-SMX-0) shows almost no activity. The different amount of adsorbed SMX on CNTs correlates to the nitrogen doping level after pyrolysis and is believed to be a major contributor to the different CO₂RR performance as observed in Fig. 5. As the adsorbed SMX amount increases, the CO₂RR performance increases. Further increase of SMX adsorption on the CNTs is limited according to the adsorption equilibrium isotherm (Fig. 2) and the low SMX solubility in water at room temperature [54].

Specifically, the FE(CO) of CNT-SMX-250 remains at above 90 % from -0.7 to -0.9 V vs RHE even if metal nanoparticles co-exist with atomic sites, as shown in Fig. 3a, 3d. Literature has revealed that exposed transition metal nanoparticles normally have a negative effect on the $\rm CO_2RR$ as they promote competing hydrogen evolution reaction

(HER) due to their strong bonding with *H [55]. The coverage of the Ni NPs by graphitic carbon layers during the CVD synthesis could help block bulk Ni from interacting with the reactants to suppress HER[33]. The utilization of the commercial CNT derived catalyst may greatly benefit from the encapsulation advantage because the CNTs have been purified by the industrial process to move bulk metal particles, thus the metal NPs left are mostly encapsulated by the CNT carbon layers, as revealed by Fig. 3a. Thus, such materials are excellent to suppress HER on the nanoparticles, indicating the commercial CNT an excellent CO_2RR carbon precursor candidate.

Electrochemistry characterizations were carried out to further investigate the electrochemical properties of each sample. The Nyquist plots by electrochemical impedance spectroscopy (EIS) are obtained as in Figure S13a, and the equivalent circuit model in the cathode compartment is defined in Figure S13b [56]. The equivalent circuit model contains solution resistance (R_S), Ohmic resistance (R_Ω), and charge-transfer resistance (R_{CT}). The charge-transfer resistance

represents the resistance for the electrons to transfer from the catalyst to the reactants. CPE_1 and CPE_2 represent the constant phase element, corresponding to the capacitance [41,57]. The fitting results shown in Table S4 reveal that CNT-SMX-250 and CNT-HT have similar solution resistance (Rs) and ohmic resistance (R $_{\Omega}$), while CNT-SMX-250 has significantly higher charge-transfer resistance (R $_{CT}$), 14 Ω versus 6 Ω , suggesting a more favorable electron transfer process at CNT-SMX-250 surface than that at CNT-HT when CO $_2$ reduction occurs. This is due to the heteroatom doping that is present in CNT-SMX-250 while absent in CNT-HT.

The double-layer capacitances ($C_{\rm dl}$) of the samples are compared in **Figure S14**. The $C_{\rm dl}$ is obtained and calculated by cyclic voltammetry (CV) in a non-Faradaic potential range from 0 to 0.3 V vs RHE (**Figure S15**) using the slope of the plots of current density differences as a function of applied potential scanning rates. CNT-SMX-250 has a larger $C_{\rm dl}$, 11.1 mF/cm², than that of CNT-HT, 7.9 mF/cm². $C_{\rm dl}$ is proportional to the electrochemical surface area (ECSA), indicating a larger ECSA of CNT-SMX-250. To further analyze CO_2RR activity of the electrochemical sites, the partial current density of CO divided by ECSA ($J_{\rm CO}$ /ECSA) has been calculated for both samples at -0.76 V vs RHE, where maximum Faradaic efficiency of CO is achieved. CNT-SMX-250 shows a $J_{\rm CO}$ /ECSA of 1.3 mA/mF, while CNT-HT only has 0.002 mA/mF. This indicates that with the incorporation of SMX adsorption for N doping, CNT-SMX-250 has a significant enhancement on the activity of the electrochemical sites.

3.3.2. Flow Cell

As revealed in Fig. 6a, the CO selectivity remains above 95 % at a wide range of current densities, from 50 to 300 mA/cm² with good repeatability. In specific, the average CO selectivity is 97.5 % at 300 mA/cm² and $-1.4\ V$ vs RHE, as revealed in Fig. 6a. This indicates an excellent CO2RR performance suitable at commercially viable production rates. The CO concentration in the flow cell effluent increases with current density while the H2 concentration remains less than 1 %, as shown in Figure S16, indicating that the catalyst could suppress HER in a wide current density range.

The stability test of CO_2RR was evaluated at 100 mA/cm² for 24 h. The CO selectivity, as revealed in Fig. 6b, decreases slightly during the 24-h stability test from 99 % to 98 % due to the slight increase of HER which competes with the CO generation [58]. The stability result is among the most stable performances reported in the literature at similar conditions [59–63]. Moreover, as revealed in Figure S16, at 300 mA/cm², the CO concentration in the effluent of cathode chamber could

reach 12%, indicating a high CO_2 conversion comparable to the state-of-the-art works operated at similar reaction conditions [6,64,65].

3.4. Nitrogen element usage

To further demonstrate the effects on nitrogen doping by the organic wastes, melamine is used as a control sample to replace SMX as the nitrogen precursor as it is a widely applied agent for nitrogen doping on the CNT surface [33,66]. Firstly, melamine at the same quantity of nitrogen element as SMX was adsorbed onto CNTs to generate CNT-Mel-250 catalyst. The as-synthesized CNT-Mel-250 in Figure S17 reveals much worse CO_2RR performance than that of CNT-SMX-250. The maximum Faradaic efficiency of CO in CNT-Mel-250 is 60.8 % compared to 91.5 % in CNT-SMX-250 at -0.76 V with a CO current density of -1 vs -14 mA/cm². The high-resolution N XPS spectrum of CNT-Mel-250 reveals no obvious N peak, indicating no N doping (Figure S10). This is possibly due to the weak π - π interaction between traditional shortchain nitrogen precursors (e.g., melamine, urea, etc.) and CNTs, leading to a very small amount of melamine being adsorbed on CNT surfaces.

To increase the loading of melamine on CNTs, CNT-Mel-excessive was synthesized by using a 10:1 melamine/carbon mass ratio for pyrolysis, and this ratio is within the range reported in literature to ensure sufficient nitrogen doping [7]. As revealed in the Figure S17, CNT-Melexcessive shows similar performance to that of CNT-SMX-250, indicating a successful nitrogen doping by melamine. The XPS spectra revealed that the nitrogen atomic concentration in CNT-Mel-excessive, 0.77 at.%, is close to that of CNT-SMX-250, 0.80 at.%. However, the total nitrogen amount used in CNT-Mel-excessive synthesis is 100 times larger than that in CNT-SMX-250, indicating a significantly higher utilization efficiency of nitrogen using SMX as the precursor, and even more sustainable when adsorbing it from a pharmaceutical waste. Since SMX and melamine has a similar decomposition temperature [67], it is probable that the nitrogen doping difference is due to SMX being adsorbed to the CNT surface by π - π interaction with multi-layers thus the metal elements on CNTs have a larger chance to form M-N bonds with the decomposed N-containing intermediates. In contrast, melamine does not fully cover the CNT surface, requiring much more melamine in the process to achieve a similar level of nitrogen doping.

We further compared the nitrogen usage in our catalyst to the literature. As shown in Table S5, CNT-SMX-250 shows significantly less (2 to 4 orders of magnitude less) nitrogen precursor usage than those in the literature, indicating an efficient and cost-effective synthesis. We also compared the $\rm CO_2RR$ performance of CNT-SMX-250 with those of Fe-

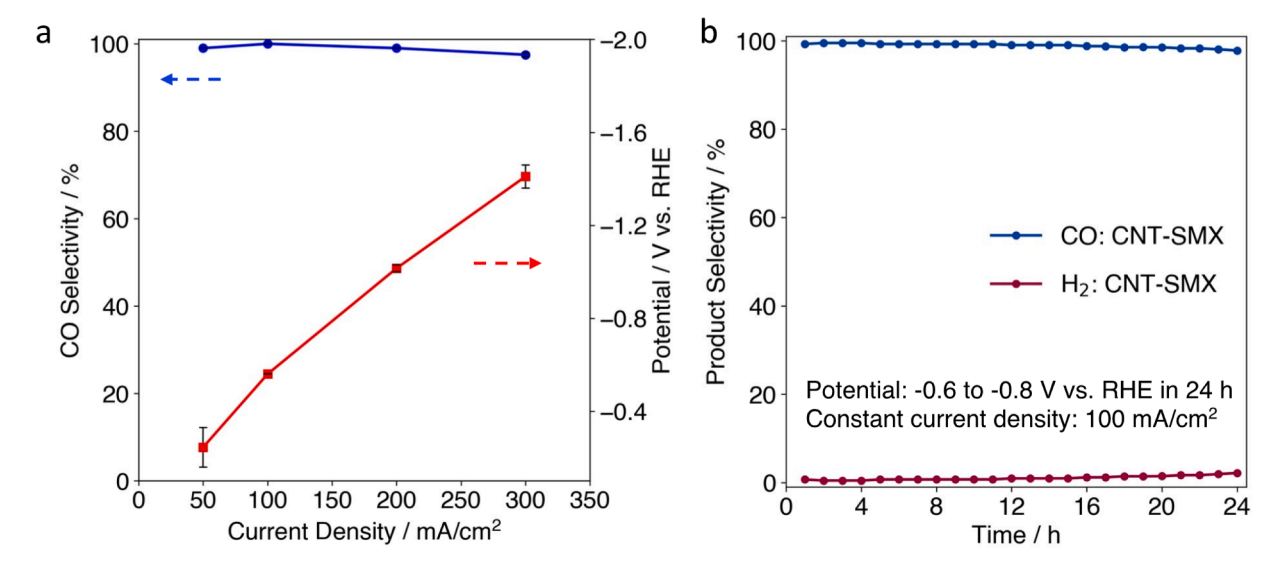


Fig. 6. (a) CO selectivity and measured potential between the cathode and reference electrode at varied current densities, (b) product selectivity of CNT-SMX-250 in the flow cell at 100 mA/cm².

based catalysts reported in the literature, as shown in Table S6. Our catalyst ranked among the top ones in terms of both FE(CO) and CO current density.

3.5. Additional experimental investigation of the active sites

In order to investigate the active sites, multiple experiments were further conducted. Firstly, ethylenediaminetetraacetic acid (EDTA) and potassium thiocyanate (KSCN), two most widely used poisoning agents to metal sites in electrolysis, were used to investigate the active site distribution in H-Cell testing. As shown in Figure S18, CNT-SMX-250 poisoned by EDTA and KSCN has a reduced CO2RR performance, indicating the poisoning of active sites to certain extent, although not completely deactivating the catalyst. As revealed in the literature, KSCN has a higher poisoning effect to metal NP than EDTA [68,69]. As a result, the different performance between EDTA- and KSCN-poisoned samples is usually an indicator of the metal NP contribution. As shown in Figure S18, both EDTA- and KSCN-poisoned samples show similar performance, suggesting no major contribution from metal NPs alone and the poisoning effects mainly occur on the single atomic Fe-N sites. This is reasonable as Ni NPs are wrapped by several carbon layers and thus are not accessible to poisons. The similar performance of CNT-SMX-250 and CNT-SMX-250-Acid (with post acid washing) also confirms no obvious metal NP contribution to CO₂RR (Figure S19).

In the literature regarding single atomic Fe—N—C or Ni—N—C catalysts, the typical metal content is around 0.2–2 wt% [70–73], which is in line with the Fe content is this work, 0.4 wt%. Nevertheless, we have conducted the experiment of introducing additional metal precursors (1 wt% of Fe to the weight of carbon by wet impregnation) along with extensive amount of melamine. As shown in Figure \$20, CNT-MeladdFe reveals even lower Faradaic efficiency and current density of CO, suggesting no additional active sites are created. This may be

because of the lower pyrolysis temperature used in this work (i.e., $650\,^{\circ}$ C) than those in the literature (typically above $800\,^{\circ}$ C as shown in Table S6) to introduce metal doping from precursors such as metal nitrates. We have also conducted an extensive-nitrogen precursor experiment, as shown in Figure S17, where CNT-Mel-extensive shows similar performance to that of CNT-SMX-250, indicating the N dopant in CNT-SMX-250 is sufficient. All the above experiments suggest that the single atomic Fe-N sites derived from intrinsic metal impurities from raw CNTs are the main active sites.

3.6. DFT investigation on the synergy between single atomic Fe-N sites and Ni NPs

Our STEM/EDS/XAS result (Fig. 3 and Fig. 4) indicates that CNT-SMX-250 catalyst is composed with Ni nanoparticles wrapped by carbon layers containing Fe and N dopants. We further performed density functional theory (DFT) calculations to gain understanding whether there exists a synergy between Ni nanoparticles and Fe-N-C that could affect CO₂RR performance. In this study, a FeN₄ moiety embedded in a graphene layer was used to model the Fe, N doped carbon because FeN₄ site was recognized as the most common site in Fe—N—C catalyst active for CO₂RR[74-76]. For comparison, we constructed atomistic models containing a FeN₄ moiety doped graphene layer with a Ni NP underneath as the support (denoted as FeN₄@Ni in Fig. 7a) and without Ni NP support (denoted as FeN₄). We employed the computational hydrogen electrode (CHE) method [77] to predict the free energy evolution along the 2e CO₂RR pathway (Fig. 7b), which involves the well-accepted *COOH and *CO as reaction intermediates. The optimized adsorption configurations of COOH and CO on FeN4@Ni site were shown in Figure S21. The limiting potential of CO₂RR, defined as the highest potential to make each electrochemical step involved exothermic, was predicted to be −0.82 V on FeN₄@Ni site and −0.61 V on FeN₄ site,

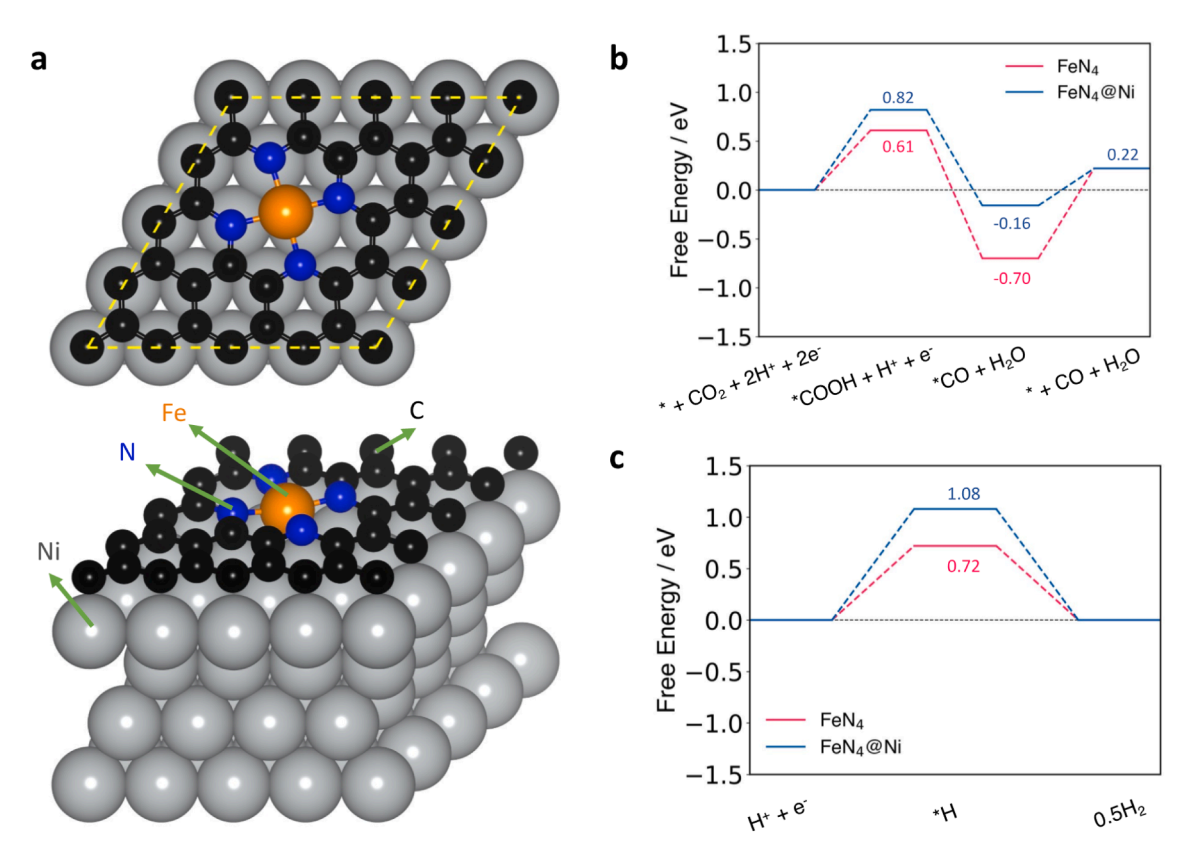


Fig. 7. (a) Atomistic structure of proposed $FeN_4@Ni$ model. In the figure, the yellow dash line represents the periodic boundary of the model, whereas the gray, blue, black, orange balls represent Ni, N, C, and Fe atoms, respectively. Calculated free energy evolution of (b) CO_2RR at the electrode potential of 0 V and (c) HER at the electrode potential of 0 V on the modeled FeN_4 sites.

respectively. In addition, the CO desorption energies were predicted to be 0.38 eV and 0.92 eV on FeN₄@Ni and FeN₄ site, respectively. Our previous study suggests that a more negative limiting potential corresponds to a more negative onset potential, and a higher CO desorption energy leads to a lower current density of CO [11]. Therefore, we predicted that FeN₄@Ni site required a more negative potential to promote CO₂RR but could generate a higher current density than FeN₄ site, in agreement with our experimental results which show that CNT-SMX-250 has the maximum FE(CO) achieved at around $-0.7 \sim -0.8$ V and CO partial current density of -14 mA/cm² at -0.76 V, while most of the state-of-the-art Fe-based catalysts having the largest FE(CO) at around $-0.5 \sim -0.6$ V [78,79]. The CO partial current density achieved by CNT-SMX-250 at around -0.8 V is larger than most of the literature at a similar applied potential, as revealed in Table S6, agreeing with the above DFT calculation.

Moreover, we predicted the free energy evolution of hydrogen evolution reaction (HER), which is a major side reaction competitive with CO₂RR, on FeN₄ sites (Fig. 7c). The limiting potential of HER was calculated to be -1.08 V on FeN₄@Ni and -0.72 V on FeN₄ site, respectively. The limiting potential difference between CO₂RR and HER, denoted as U_I(CO₂RR)-U_I(HER), is used as a descriptor to gauge the selectivity of a catalyst for CO₂ reduction, and a large, positive value of U_I(CO₂RR)-U_I(HER) indicates a high selectivity toward CO₂ reduction [80]. We calculated the value of $U_L(CO_2RR)$ - $U_L(HER)$ to be 0.26 V on FeN₄@Ni site and 0.11 V on FeN₄ site, respectively, implying that both FeN₄ sites on the two structures show good selectivity of CO₂RR over HER while the hybrid structure Fe-N₄@Ni shows slightly higher CO selectivity than that of FeN₄ alone. These DFT predictions are consistent with the experimental observation that CNT-SMX-250 shows a high CO Faradaic efficiency of 91.5 %. Overall, the DFT calculations predict that FeN₄ sites containing carbon layers on Ni nanoparticles as the substrate could boost the production rate of CO2RR with a high CO selectivity compared with FeN₄ sites alone, despite a small sacrifice on the applied potential, a slight increase in energy consumption.

In summary, the experimental and theoretical investigations have revealed that the high performance of CNT-SMX-250 in this work is contributed by two major factors. The first major contribution is the existence of single atomic sites (primarily Fe). Secondly, the synergetic effect between Ni NP and Fe-N-C also promotes the CO₂RR reaction rate and CO selectivity by lowering the CO* desorption energy barrier as predicted by the DFT calculations. The multiple contributions to enhanced CO₂RR performance suggest the advantage of using commercial CNTs and their intrinsic metal impurities to generate active metal active sites. A possible reason is that the commercial CNTs have gone through industrial process of removing the majority of exposed metal nanoparticles and unstable metal phases, leaving the most rigid and stable metal sites on the CNT surfaces. These metal sites are efficient in adsorbing SMX from the solution and form active M-N-C sites at a lower pyrolysis temperature. Based on the results in this work, this method shows a much higher nitrogen precursor utilization than in the literature (Table S5).

4. Conclusion

In summary, we directly utilized commercial multi-walled carbon nanotubes to adsorb pharmaceutical wastes such as SMX and transformed the mixture to an efficient CO₂RR catalyst through a simple synthesis process. The metal impurities in commercial CNTs bond with nitrogen from SMX to form single atomic M—N—C sites that are active for CO₂RR. These single atomic sites were dominated by Fe, while Ni nanoparticles also exist but are generally not active due to encapsulation by carbon layers. Interestingly, DFT calculations suggest the existence of a synergetic effect between Fe atomic sites and Ni NPs that promote the CO₂RR performance by lowering the *CO desorption energy, thus increasing the CO partial current density. The CNT-SMX-250 catalyst achieved excellent H-Cell performance that is among top ones reported

in the leading literature. In a flow cell testing, the CNT-SMX-250 catalyst reached $300 \, \text{mA/cm}^2$ of total current density with a CO selectivity larger than $97.5 \, \%$. The catalyst also delivers a stable performance at a fixed current density of $100 \, \text{mA/cm}^2$ for 24 h. Furthermore, the nitrogen utilization rate of SMX in this synthesis method is significantly higher than that using conventional nitrogen precursor, melamine, to achieve a similar level of nitrogen doping and CO_2RR performance. More importantly, this synthesis method converts a waste to a useful product, and it does not require any metal precursors or additional pre- or post-treatment to produce the efficient catalyst, thus a truly environmentally benign and cost-effective method.

Declaration of Competing Interest

The authors declare that they have no known competing financial interests or personal relationships that could have appeared to influence the work reported in this paper.

Data availability

Data will be made available on request.

Acknowledgements

This work was supported by the U.S. National Science Foundation (NSF CBET #1805132). The use of Materials Characterization Facility (MCF) at Texas A&M University is acknowledged (RRID: SCR_022202). The use of Advanced Photon Source, an Office of Science User Facility operated for the U.S. Department of Energy (DOE) Office of Science by Argonne National Laboratory is supported by the U.S. DOE under Contract DE-AC02-06CH11357.

Appendix A. Supplementary data Adsorption isotherm models, selectivity calculation, computational methods, additional SEM, TEM, EDS, BET, XPS, XRD, equivalent circuit, ECSA, H-Cell performance, DFT models, and performance caparison.

Supplementary data to this article can be found online at https://doi.org/10.1016/j.cej.2022.139712.

References:

- J. Qiao, Y. Liu, F. Hong, J. Zhang, A review of catalysts for the electroreduction of carbon dioxide to produce low-carbon fuels, Chem Soc Rev 43 (2014) 631–675.
- [2] D.D. Zhu, J.L. Liu, S.Z. Qiao, Recent Advances in Inorganic Heterogeneous Electrocatalysts for Reduction of Carbon Dioxide, Adv Mater 28 (2016) 3423–3452.
- [3] A.S. Varela, W. Ju, A. Bagger, P. Franco, J. Rossmeisl, P. Strasser, Electrochemical reduction of CO2 on metal-nitrogen-doped carbon catalysts, ACS Catal. 9 (2019) 7270–7284.
- [4] M. Li, H. Wang, W. Luo, P.C. Sherrell, J. Chen, J. Yang, Heterogeneous Single-Atom Catalysts for Electrochemical CO2 Reduction Reaction, Adv Mater 32 (2020) e2001848
- [5] Y. Gang, F. Pan, Y. Fei, Z. Du, Y.H. Hu, Y. Li, Highly Efficient Nickel, Iron and Nitrogen Co-Doped Carbon Catalysts Derived from Industrial Waste Petroleum Coke for Electrochemical CO2 Reduction, ACS Sustainable Chem. Eng. 8 (2020) 8840–8847.
- [6] T. Zheng, K. Jiang, N. Ta, Y. Hu, J. Zeng, J. Liu, H. Wang, Large-Scale and Highly Selective CO2 Electrocatalytic Reduction on Nickel Single-Atom Catalyst, Joule 3 (2019) 265–278.
- [7] F. Pan, B. Li, E. Sarnello, Y. Fei, Y. Gang, X. Xiang, Z. Du, P. Zhang, G. Wang, H. T. Nguyen, T. Li, Y.H. Hu, H.C. Zhou, Y. Li, Atomically Dispersed Iron-Nitrogen Sites on Hierarchically Mesoporous Carbon Nanotube and Graphene Nanoribbon Networks for CO2 Reduction, ACS Nano 14 (2020) 5506–5516.
- [8] F. Pan, B. Li, E. Sarnello, S. Hwang, Y. Gang, X. Feng, X. Xiang, N.M. Adli, T. Li, D. Su, Boosting CO2 reduction on Fe-NC with sulfur incorporation: Synergistic electronic and structural engineering, Nano Energy 68 (2020), 104384.
- [9] F. Pan, H. Zhang, Z. Liu, D. Cullen, K. Liu, K. More, G. Wu, G. Wang, Y. Li, Atomic-level active sites of efficient imidazolate framework-derived nickel catalysts for CO 2 reduction, J. Mater. Chem. A 7 (2019) 26231–26237.
- [10] J. Pellessier, Y. Gang, Y. Li, A Sustainable Synthesis of Nickel-Nitrogen-Carbon Catalysts for Efficient Electrochemical CO2 Reduction to CO, ES Materials & Manufacturing (2021).

- [11] F. Pan, B. Li, E. Sarnello, Y. Fei, Y. Gang, X. Xiang, Z. Du, P. Zhang, G. Wang, H. T. Nguyen, Atomically dispersed iron–nitrogen sites on hierarchically mesoporous carbon nanotube and graphene nanoribbon networks for CO2 reduction, ACS Nano 14 (2020) 5506–5516.
- [12] F. Pan, B. Li, E. Sarnello, Y. Fei, X. Feng, Y. Gang, X. Xiang, L. Fang, T. Li, Y.H. Hu, Pore-edge tailoring of single-atom iron-nitrogen sites on graphene for enhanced CO2 reduction, Acs Catal 10 (2020) 10803–10811.
- [13] W. Ju, A. Bagger, G.-P. Hao, A.S. Varela, I. Sinev, V. Bon, B. Roldan Cuenya, S. Kaskel, J. Rossmeisl, P. Strasser, Understanding activity and selectivity of metalnitrogen-doped carbon catalysts for electrochemical reduction of CO2, Nature Communications 8 (2017) 1–9.
- [14] S. Ma, P. Su, W. Huang, S.P. Jiang, S. Bai, J. Liu, Atomic Ni species anchored N-doped carbon hollow spheres as nanoreactors for efficient electrochemical CO2 reduction, ChemCatChem 11 (2019) 6092–6098.
- [15] J. Leverett, R. Daiyan, L. Gong, K. Iputera, Z. Tong, J. Qu, Z. Ma, Q. Zhang, S. Cheong, J. Cairney, Designing Undercoordinated Ni–N x and Fe–N x on Holey Graphene for Electrochemical CO2 Conversion to Syngas, ACS Nano 15 (2021) 12006–12018.
- [16] H. Zhang, J. Li, S. Xi, Y. Du, X. Hai, J. Wang, H. Xu, G. Wu, J. Zhang, J. Lu, J. Wang, A Graphene-Supported Single-Atom FeN5 Catalytic Site for Efficient Electrochemical CO2 Reduction, Angew Chem Int Ed Engl 58 (2019) 14871–14876
- [17] X. Zhang, Y. Wang, M. Gu, M. Wang, Z. Zhang, W. Pan, Z. Jiang, H. Zheng, M. Lucero, H. Wang, Molecular engineering of dispersed nickel phthalocyanines on carbon nanotubes for selective CO2 reduction, Nature, Energy 5 (2020) 684–692.
- [18] Q. Zhang, Y. Zhang, J. Mao, J. Liu, Y. Zhou, D. Guay, J. Qiao, Electrochemical reduction of CO2 by SnOx nanosheets anchored on multiwalled carbon nanotubes with tunable functional groups, ChemSusChem 12 (2019) 1443–1450.
- [19] Y. Cheng, S. Zhao, B. Johannessen, J.P. Veder, M. Saunders, M.R. Rowles, M. Cheng, C. Liu, M.F. Chisholm, R. De Marco, Atomically dispersed transition metals on carbon nanotubes with ultrahigh loading for selective electrochemical carbon dioxide reduction, Adv. Mater. 30 (2018) 1706287.
- [20] Z. Sui, Q. Meng, X. Zhang, R. Ma, B. Cao, Green synthesis of carbon nanotube–graphene hybrid aerogels and their use as versatile agents for water purification, J. Mater. Chem. 22 (2012) 8767–8771.
- [21] C.W. Tan, K.H. Tan, Y.T. Ong, A.R. Mohamed, S.H.S. Zein, S.H. Tan, Energy and environmental applications of carbon nanotubes, Environ. Chem. Lett. 10 (2012) 265–273.
- [22] P.P. Sharma, J. Wu, R.M. Yadav, M. Liu, C.J. Wright, C.S. Tiwary, B.I. Yakobson, J. Lou, P.M. Ajayan, X.D. Zhou, Nitrogen-doped carbon nanotube arrays for high-efficiency electrochemical reduction of CO2: on the understanding of defects, defect density, and selectivity, Angew. Chem. 127 (2015) 13905–13909.
- [23] F. Pan, H. Zhao, W. Deng, X. Feng, Y. Li, A novel N, Fe-Decorated carbon nanotube/carbon nanosheet architecture for efficient CO2 reduction, Electrochim. Acta 273 (2018) 154-161.
- [24] C. Ma, P. Hou, X. Wang, Z. Wang, W. Li, P. Kang, Carbon nanotubes with rich pyridinic nitrogen for gas phase CO2 electroreduction, Appl Catal B-Environ 250 (2019) 347–354.
- [25] Y. Yao, B. Gao, H. Chen, L. Jiang, M. Inyang, A.R. Zimmerman, X. Cao, L. Yang, Y. Xue, H. Li, Adsorption of sulfamethoxazole on biochar and its impact on reclaimed water irrigation, J. Hazard. Mater. 209 (2012) 408–413.
- [26] T. Garoma, S.K. Umamaheshwar, A. Mumper, Removal of sulfadiazine, sulfamethizole, sulfamethoxazole, and sulfathiazole from aqueous solution by ozonation, Chemosphere 79 (2010) 814–820.
- [27] Y.H. Li, Y.M. Zhao, W.B. Hu, I. Ahmad, Y.Q. Zhu, X.J. Peng, Z.K. Luan, Carbon nanotubes - the promising adsorbent in wastewater treatment, J. Phys.: Conf. Ser. 61 (2007) 698–702.
- [28] Z. Yin, C. Cui, H. Chen, X. Duoni, W.Q. Yu, The Application of Carbon Nanotube/ Graphene-Based Nanomaterials in Wastewater Treatment, Small 16 (2020) 1902301
- [29] C.-Y. Lin, S.-D. Huang, Application of liquid–liquid–liquid microextraction and high-performance liquid-chromatography for the determination of sulfonamides in water, Anal. Chim. Acta 612 (2008) 37–43.
- [30] B. Zhang, J. Zhang, J. Shi, D. Tan, L. Liu, F. Zhang, C. Lu, Z. Su, X. Tan, X. Cheng, Manganese acting as a high-performance heterogeneous electrocatalyst in carbon dioxide reduction, Nat. Commun. 10 (2019) 1–8.
- [31] F. Pan, B. Li, X. Xiang, G. Wang, Y. Li, Efficient CO2 electroreduction by highly dense and active pyridinic nitrogen on holey carbon layers with fluorine engineering, Acs Catal 9 (2019) 2124–2133.
- [32] H. Zhang, J. Li, S. Xi, Y. Du, X. Hai, J. Wang, H. Xu, G. Wu, J. Zhang, J. Lu, J. Wang, A Graphene-Supported Single-Atom FeN5 Catalytic Site for Efficient Electrochemical CO2 Reduction, Angew. Chem. 131 (2019) 15013–15018.
- [33] Y. Gang, E. Sarnello, J. Pellessier, S. Fang, M. Suarez, F. Pan, Z. Du, P. Zhang, L. Fang, Y. Liu, T. Li, H.-C. Zhou, Y.H. Hu, Y. Li, One-Step Chemical Vapor Deposition Synthesis of Hierarchical Ni and N Co-Doped Carbon Nanosheet/ Nanotube Hybrids for Efficient Electrochemical CO2 Reduction at Commercially Viable Current Densities, ACS Catal. 11 (2021) 10333–10344.
- [34] Y. Yao, Y. Zhang, B. Gao, R. Chen, F. Wu, Removal of sulfamethoxazole (SMX) and sulfapyridine (SPY) from aqueous solutions by biochars derived from anaerobically digested bagasse, Environ. Sci. Pollut. Res. 25 (2018) 25659–25667.
- [35] S. Zeng, Y.-K. Choi, E. Kan, Iron-activated bermudagrass-derived biochar for adsorption of aqueous sulfamethoxazole: Effects of iron impregnation ratio on biochar properties, adsorption, and regeneration, Sci. Total Environ. 750 (2021), 141691.

- [36] H.M. Jang, S. Yoo, S. Park, E. Kan, Engineered biochar from pine wood: Characterization and potential application for removal of sulfamethoxazole in water, Environ. Eng. Res. 24 (2019) 608–617.
- [37] H. Valencia, A. Gil, G. Frapper, Trends in the hydrogen activation and storage by adsorbed 3d transition metal atoms onto graphene and nanotube surfaces: A DFT study and molecular orbital analysis, The Journal of Physical Chemistry C 119 (2015) 5506–5522.
- [38] J.-C. Li, P.-X. Hou, S.-Y. Zhao, C. Liu, D.-M. Tang, M. Cheng, F. Zhang, H.-M. Cheng, A 3D bi-functional porous N-doped carbon microtube sponge electrocatalyst for oxygen reduction and oxygen evolution reactions, Energ Environ Sci 9 (2016) 3079–3084.
- [39] Y. Hou, Y.-L. Liang, P.-C. Shi, Y.-B. Huang, R. Cao, Atomically dispersed Ni species on N-doped carbon nanotubes for electroreduction of CO2 with nearly 100% CO selectivity, Appl. Catal. B 271 (2020), 118929.
- [40] B.H. Suryanto, T. Fang, S. Cheong, R.D. Tilley, C. Zhao, From the inside-out: leached metal impurities in multiwall carbon nanotubes for purification or electrocatalysis, J. Mater. Chem. A 6 (2018) 4686–4694.
- [41] F. Pan, B. Li, W. Deng, Z. Du, Y. Gang, G. Wang, Y. Li, Promoting electrocatalytic CO2 reduction on nitrogen-doped carbon with sulfur addition, Appl Catal B-Environ 252 (2019) 240–249.
- [42] Z. Yang, Z. Yao, G. Li, G. Fang, H. Nie, Z. Liu, X. Zhou, X.a. Chen, S. Huang, Sulfur-Doped Graphene as an Efficient Metal-free Cathode Catalyst for Oxygen Reduction, ACS Nano, 6 (2012) 205-211.
- [43] Y. Ito, W. Cong, T. Fujita, Z. Tang, M. Chen, High Catalytic Activity of Nitrogen and Sulfur Co-Doped Nanoporous Graphene in the Hydrogen Evolution Reaction, Angew. Chem. 127 (2015) 2159–2164.
- [44] K. Li, S. Zhang, X. Zhang, S. Liu, H. Jiang, T. Jiang, C. Shen, Y. Yu, W. Chen, Atomic Tuning of Single-Atom Fe-N-C Catalysts with Phosphorus for Robust Electrochemical CO2 Reduction, Nano Lett. 22 (2022) 1557–1565.
- [45] P. Zimmermann, D. Ar, M. Rößler, P. Holze, B. Cula, C. Herwig, C. Limberg, Selective Transformation of Nickel-Bound Formate to CO or C— C Coupling Products Triggered by Deprotonation and Steered by Alkali-Metal Ions, Angew. Chem. 133 (2021) 2342–2351.
- [46] K. Lakshmanan, W.H. Huang, S.A. Chala, B.W. Taklu, E.A. Moges, J.F. Lee, P. Y. Huang, Y.C. Lee, M.C. Tsai, W.N. Su, Highly Active Oxygen Coordinated Configuration of Fe Single-Atom Catalyst toward Electrochemical Reduction of CO2 into Multi-Carbon Products, Adv Funct Mater 2109310 (2022).
- [47] S. Paul, Y.-L. Kao, L. Ni, R. Ehnert, I. Herrmann-Geppert, R. van de Krol, R. W. Stark, W. Jaegermann, U.I. Kramm, P. Bogdanoff, Influence of the metal center in M-N-C catalysts on the CO2 reduction reaction on gas diffusion electrodes, Acs Catal 11 (2021) 5850–5864.
- [48] X. Li, X. Huang, S. Xi, S. Miao, J. Ding, W. Cai, S. Liu, X. Yang, H. Yang, J. Gao, Single cobalt atoms anchored on porous N-doped graphene with dual reaction sites for efficient Fenton-like catalysis, J. Am. Chem. Soc. 140 (2018) 12469–12475.
- [49] K. Jiang, S. Siahrostami, T. Zheng, Y. Hu, S. Hwang, E. Stavitski, Y. Peng, J. Dynes, M. Gangisetty, D. Su, Isolated Ni single atoms in graphene nanosheets for highperformance CO 2 reduction, Energ, Environ Sci 11 (2018) 893–903.
- [50] Y. Pan, Y. Chen, K. Wu, Z. Chen, S. Liu, X. Cao, W.-C. Cheong, T. Meng, J. Luo, L. Zheng, C. Liu, D. Wang, Q. Peng, J. Li, C. Chen, Regulating the coordination structure of single-atom Fe-NxCy catalytic sites for benzene oxidation, Nat. Commun. 10 (2019) 4290.
- [51] Á. García, L. Pascual, P. Ferrer, D. Gianolio, G. Held, D.C. Grinter, M.A. Peña, M. Retuerto, S. Rojas, Study of the evolution of FeNxCy and Fe3C species in Fe/N/C catalysts during the oxygen reduction reaction in acid and alkaline electrolyte, J. Power Sources 490 (2021), 229487.
- [52] A. Zitolo, V. Goellner, V. Armel, M.-T. Sougrati, T. Mineva, L. Stievano, E. Fonda, F. Jaouen, Identification of catalytic sites for oxygen reduction in iron-and nitrogen-doped graphene materials, Nat. Mater. 14 (2015) 937–942.
- [53] C. Wang, X. Hu, X. Hu, X. Liu, Q. Guan, R. Hao, Y. Liu, W. Li, Typical transition metal single-atom catalysts with a metal-pyridine N structure for efficient CO2 electroreduction, Appl Catal B-Environ 296 (2021), 120331.
- [54] R. Dahlan, C. Mcdonald, V.B. Sunderland, Solubilities and intrinsic dissolution rates of sulphamethoxazole and trimethoprim, J. Pharm. Pharmacol. 39 (1987) 246–251.
- [55] F. Pan, Y. Yang, Designing CO 2 reduction electrode materials by morphology and interface engineering, Energy Environ. Sci. 13 (2020) 2275–2309.
- [56] D.H. Won, H. Shin, J. Koh, J. Chung, H.S. Lee, H. Kim, S.I. Woo, Highly Efficient, Selective, and Stable CO2 Electroreduction on a Hexagonal Zn Catalyst, Angew. Chem. Int. Ed. 55 (2016) 9297–9300.
- [57] D.H. Won, H. Shin, J. Koh, J. Chung, H.S. Lee, H. Kim, S.I. Woo, Highly efficient, selective, and stable CO2 electroreduction on a hexagonal Zn catalyst, Angew. Chem. 128 (2016) 9443–9446.
- [58] A. Goyal, G. Marcandalli, V.A. Mints, M.T.M. Koper, Competition between CO2 Reduction and Hydrogen Evolution on a Gold Electrode under Well-Defined Mass Transport Conditions, J. Am. Chem. Soc. 142 (2020) 4154–4161.
- [59] X. Wang, X. Li, S. Ding, Y. Chen, Y. Liu, M. Fang, G. Xiao, Y. Zhu, Constructing ample active sites in nitrogen-doped carbon materials for efficient electrocatalytic carbon dioxide reduction, Nano Energy 90 (2021), 106541.
- [60] J. Huang, S. Chen, F. Yang, W. Yu, Q. Meng, H. Yu, Z. Zeng, J. Wang, S. Deng, Nickel Nanoparticles with Narrow Size Distribution Confined in Nitrogen-Doped Carbon for Efficient Reduction of CO2 to CO, Catal. Lett. 152 (2022) 600–609.
- [61] M. Duarte, N. Daems, J. Hereijgers, D. Arenas-Esteban, S. Bals, T. Breugelmans, Enhanced CO2 electroreduction with metal-nitrogen-doped carbons in a continuous flow reactor, J. CO2 Util. 50 (2021), 101583.

- [62] F. Yang, H. Yu, X. Mao, Q. Meng, S. Chen, Q. Deng, Z. Zeng, J. Wang, S. Deng, Boosting electrochemical CO2 reduction on ternary heteroatoms-doped porous carbon, Chem. Eng. J. 425 (2021), 131661.
- [63] M. Li, C. Yan, R. Ramachandran, Y. Lan, H. Dai, H. Shan, X. Meng, D. Cui, F. Wang, Z.-X. Xu, Non-peripheral octamethyl-substituted cobalt phthalocyanine nanorods supported on N-doped reduced graphene oxide achieve efficient electrocatalytic CO2 reduction to CO, Chem. Eng. J. 430 (2022), 133050.
- [64] E. Jeng, F. Jiao, Investigation of CO 2 single-pass conversion in a flow electrolyzer, React. Chem. Eng. 5 (2020) 1768–1775.
- [65] Y. Zhang, K. Qi, J. Li, B.A. Karamoko, L. Lajaunie, F. Godiard, E. Oliviero, X. Cui, Y. Wang, Y. Zhang, H. Wu, W. Wang, D. Voiry, 2.6% cm–2 Single-Pass CO2-to-CO Conversion Using Ni Single Atoms Supported on Ultra-Thin Carbon Nanosheets in a Flow Electrolyzer, ACS Catal. 11 (2021) 12701–12711.
- [66] C. Ding, C. Feng, Y. Mei, F. Liu, H. Wang, M. Dupuis, C. Li, Carbon nitride embedded with transition metals for selective electrocatalytic CO2 reduction, Appl Catal B-Environ 268 (2020), 118391.
- [67] C. Garnero, V. Aiassa, M. Longhi, Sulfamethoxazole:hydroxypropyl-β-cyclodextrin complex: preparation and characterization, J. Pharm. Biomed. Anal. 63 (2012) 74–79
- [68] M. Ma, G. Li, W. Yan, Z. Wu, Z. Zheng, X. Zhang, Q. Wang, G. Du, D. Liu, Z. Xie, Single-Atom Molybdenum Engineered Platinum Nanocatalyst for Boosted Alkaline Hydrogen Oxidation, Adv. Energy Mater. 12 (2022) 2103336.
- [69] B. Lu, L. Guo, F. Wu, Y. Peng, J.E. Lu, T.J. Smart, N. Wang, Y.Z. Finfrock, D. Morris, P. Zhang, Ruthenium atomically dispersed in carbon outperforms platinum toward hydrogen evolution in alkaline media, Nat. Commun. 10 (2019) 1–11.
- [70] Y. Wang, B.J. Park, V.K. Paidi, R. Huang, Y. Lee, K.-J. Noh, K.-S. Lee, J.W. Han, Precisely constructing orbital coupling-modulated dual-atom fe pair sites for synergistic CO2 electroreduction, Acs Energy Lett 7 (2022) 640–649.
- [71] L. Lin, H. Li, Y. Wang, H. Li, P. Wei, B. Nan, R. Si, G. Wang, X. Bao, Temperature-Dependent CO2 Electroreduction over Fe-N-C and Ni-N-C Single-Atom Catalysts, Angew. Chem. 133 (2021) 26786–26790.

- [72] Z. Li, R. Wu, S. Xiao, Y. Yang, L. Lai, J.S. Chen, Y. Chen, Axial chlorine coordinated iron-nitrogen-carbon single-atom catalysts for efficient electrochemical CO2 reduction, Chem. Eng. J. 430 (2022), 132882.
- [73] F. Wang, Z. Miao, J. Mu, Y. Zhao, M. Liang, J. Meng, X. Wu, P. Zhou, J. Zhao, S. Zhuo, A Ni nanoparticles encapsulated in N-doped carbon catalyst for efficient electroreduction CO2: Identification of active sites for adsorption and activation of CO2 molecules, Chem. Eng. J. 428 (2022), 131323.
- [74] K.X. Liu, S. Kattel, V. Mao, G.F. Wang, Electrochemical and Computational Study of Oxygen Reduction Reaction on Nonprecious Transition Metal/Nitrogen Doped Carbon Nanofibers in Acid Medium, J Phys Chem C 120 (2016) 1586–1596.
- [75] G. Wu, K.L. More, C.M. Johnston, P. Zelenay, High-performance electrocatalysts for oxygen reduction derived from polyaniline, iron, and cobalt, Science 332 (2011) 443–447.
- [76] A. Zitolo, V. Goellner, V. Armel, M.T. Sougrati, T. Mineva, L. Stievano, E. Fonda, F. Jaouen, Identification of catalytic sites for oxygen reduction in iron- and nitrogen-doped graphene materials, Nat Mater 14 (2015) 937–942.
- [77] J.K. Norskov, J. Rossmeisl, A. Logadottir, L. Lindqvist, J.R. Kitchin, T. Bligaard, H. Jonsson, Origin of the overpotential for oxygen reduction at a fuel-cell cathode, J Phys Chem B 108 (2004) 17886–17892.
- [78] F. Pan, W. Deng, C. Justiniano, Y. Li, Identification of champion transition metals centers in metal and nitrogen-codoped carbon catalysts for CO2 reduction, Appl. Catal. B 226 (2018) 463–472.
- [79] W. Ren, X. Tan, W. Yang, C. Jia, S. Xu, K. Wang, S.C. Smith, C. Zhao, Isolated diatomic Ni-Fe metal–nitrogen sites for synergistic electroreduction of CO2, Angew. Chem. Int. Ed. 58 (2019) 6972–6976.
- [80] X. Li, W. Bi, M. Chen, Y. Sun, H. Ju, W. Yan, J. Zhu, X. Wu, W. Chu, C. Wu, Y. Xie, Exclusive Ni–N4 Sites Realize Near-Unity CO Selectivity for Electrochemical CO2 Reduction, J. Am. Chem. Soc. 139 (2017) 14889–14892.